AGU PUBLICATIONS

JGR

Journal of Geophysical Research: Space Physics

RESEARCH ARTICLE
10.1002/2014JA020462

Key Points:
- Thirty-eight percent of magnetic perturbation variance captured by mean + 3 modes of variability
- Modes of variability differ between winter and summer hemispheres
- Modes 1 and 3 are well correlated with interplanetary magnetic field parameters

Correspondence to:
E. D. P. Cousins,
ecousins@ucar.edu

Citation:
Cousins, E. D. P., T. Matsuo, A. D. Richmond, and B. J. Anderson (2015), Dominant modes of variability in large-scale Birkeland currents, *J. Geophys. Res. Space Physics*, *120*, 6722–6735, doi:10.1002/2014JA020462.

Received 6 AUG 2014
Accepted 16 JUN 2015
Accepted article online 18 JUN 2015
Published online 7 AUG 2015

Dominant modes of variability in large-scale Birkeland currents

E. D. P. Cousins[1], Tomoko Matsuo[2,3], A. D. Richmond[1], and B. J. Anderson[4]

[1]High Altitude Observatory, National Center for Atmospheric Research, Boulder, Colorado, USA, [2]Cooperative Institute for Research in Environmental Sciences, University of Colorado Boulder, Boulder, Colorado, USA, [3]Space Weather Prediction Center, National Oceanic and Atmospheric Administration, Boulder, Colorado, USA, [4]The Johns Hopkins University Applied Physics Laboratory, Laurel, Maryland, USA

Abstract Properties of variability in large-scale Birkeland currents are investigated through empirical orthogonal function (EOF) analysis of 1 week of data from the Active Magnetosphere and Planetary Electrodynamics Response Experiment (AMPERE). Mean distributions and dominant modes of variability are identified for both the Northern and Southern Hemispheres. Differences in the results from the two hemispheres are observed, which are attributed to seasonal differences in conductivity (the study period occurred near solstice). A universal mean and set of dominant modes of variability are obtained through combining the hemispheric results, and it is found that the mean and first three modes of variability (EOFs) account for 38% of the total observed squared magnetic perturbations (δB^2) from both hemispheres. The mean distribution represents a standard Region 1/Region 2 (R1/R2) morphology of currents and EOF 1 captures the strengthening/weakening of the average distribution and is well correlated with the north-south component of the interplanetary magnetic field (IMF). EOF 2 captures a mixture of effects including the expansion/contraction and rotation of the (R1/R2) currents; this mode correlates only weakly with possible external driving parameters. EOF 3 captures changes in the morphology of the currents in the dayside cusp region and is well correlated with the dawn-dusk component of the IMF. The higher-order EOFs capture more complex, smaller-scale variations in the Birkeland currents and appear generally uncorrelated with external driving parameters. The results of the EOF analysis described here are used for describing error covariance in a data assimilation procedure utilizing AMPERE data, as described in a companion paper.

1. Introduction

An important agent of solar wind-magnetosphere-ionosphere (SW-MI) coupling is the Birkeland current system, which consists of currents flowing from the magnetosphere along geomagnetic field lines to close through the high-latitude ionosphere in both hemispheres. Knowledge of the complete properties of this current system is of great utility for understanding and specifying the energy inputs to the upper atmosphere in the high-latitude regions and is an important diagnostic of magnetospheric processes.

Magnetic observations from a variety of satellites including TRIAD [e.g., *Iijima and Potemra*, 1976], Dynamics Explorer (DE) 2 [e.g., *Weimer*, 2001a, 2005], Ørsted and Magsat [e.g., *Papitashvili et al.*, 2002; *Christiansen et al.*, 2002], Challenging Minisatellite Payload (CHAMP) [e.g., *Wang et al.*, 2005], and Iridium [e.g., *Anderson et al.*, 2008; *Green et al.*, 2009] have enabled statistical studies and empirical modeling of these field-aligned currents (FACs). These studies have elucidated the typical configuration of FACs and their typical dependence on solar wind conditions and season. More recently, the Active Magnetosphere and Planetary Electrodynamics Response Experiment (AMPERE), which makes use of magnetometer data from the Iridium communication satellite constellation [*Korth et al.*, 2010; *Anderson et al.*, 2014], has enabled estimation of the global FAC distribution on 10 min timescales, allowing for studies of the time evolution of the current system [e.g., *Clausen et al.*, 2013; *Merkin et al.*, 2013; *Anderson et al.*, 2014].

AMPERE data are analyzed in this study using the technique of empirical orthogonal functions (EOFs). This EOF analysis is a variant of principal component analysis (PCA) that utilizes a nonlinear regression analysis and, unlike traditional PCA, can be applied to sparse data that are not regularly gridded. PCA or EOF analysis enables the identification of dominant modes of variability in a data set and enables representation of large-scale components of the data in a small number of basis functions (i.e., dimensionality reduction). The EOF technique used in this study has been successfully applied to other high-latitude ionospheric data

sets, including DE-2 electric fields [*Matsuo et al.*, 2002] and Super Dual Auroral Radar Network (SuperDARN) plasma drifts [*Cousins et al.*, 2013]. Generally speaking, the significant advantage that this technique has over the more traditional approach of binning by driving parameters and spherical harmonic fitting is that it allows the data to speak for themselves, in that it makes fewer assumptions regarding the drivers and the functional form of the data.

In this study, statistical properties of variability in FACs are investigated using EOFs derived from 1 week of AMPERE data. Correlations between the dominant modes of variability and possible external driving conditions are tested, and the contribution of these modes to the total observed variance in the data is quantified. The derived EOFs are additionally used to visualize and quantify spatial correlations in FACs and magnetic perturbations. Furthermore, the EOFs derived in this study are used as the basis of a background error covariance model in an assimilation procedure utilizing AMPERE data, as described in a companion paper [*Cousins et al.*, 2015], referred to hereafter as Paper 2. Without the covariance matrix estimated through the EOF analysis described in this paper, it would be necessary to prescribe a covariance matrix, based on qualitative assumptions, in order to ingest AMPERE data into a data assimilation method. The data assimilation method is motivated and described in Paper 2.

The AMPERE data and the method of calculating EOFs are described in section 2, and the properties of the derived EOFs are described in section 3. A comparison of the results to those of previous studies and possible geophysical interpretations of the results are discussed in section 4.

2. Technique

2.1. AMPERE Data Set

AMPERE data originate from engineering magnetometers on board Iridium spacecraft. The Iridium constellation consists of 66 satellites (and additional on-orbit spares) in six orbital planes in circular polar orbits at 780 km altitude. This configuration results in 12 cuts in local time that are visited by different spacecraft at a time cadence of 9 min. Due to the offset between the Earth's geographic and magnetic poles, the spacecraft orbits can each sample many hours of magnetic local time (MLT), providing coverage of the majority of the auroral and polar regions over the course of a day. In the standard mode, magnetometer data are acquired from all spacecraft at a sampling interval of 19.4 s/sample, resulting in a spatial resolution of ~1°; in a high-rate mode, this sampling interval is decreased to 2.16 s/sample, resulting in a ~0.1° resolution.

The Iridium magnetometer data are processed by the AMPERE Science Data Center to adjust for satellite attitude, subtract the Earth's main geomagnetic field, and apply long-period detrending [*Korth et al.*, 2010; *Anderson et al.*, 2014], resulting in magnetic perturbation vectors. For this study, the spacecraft locations and magnetic perturbation vectors are mapped into Modified Apex Coordinates referenced to 110 km altitude (as defined by *Richmond* [1995]) (referred to hereafter as APEX coordinates), following the method described by *Knipp et al.* [2014]. Only data from locations poleward of ±45° latitude and only the two horizontal components (approximately magnetic eastward and equatorward) of the vector magnetic perturbations are retained for analysis.

For this study, AMPERE data are obtained for the week of 26 November through 2 December 2011, during which high-rate data were available (and included) for 1 day (29 November). Figure 1 shows the geomagnetic and interplanetary conditions during this week. The interplanetary magnetic field (IMF) and solar wind velocity data are obtained from the 1 min resolution OMNI data set [*King and Papitashvili*, 2005] and are smoothed with a 45 min averaging window but are not time shifted. Quiet geomagnetic conditions persisted throughout the majority of the week, with some enhancements in geomagnetic activity occurring following the arrival of a weak disturbance in the interplanetary medium near the middle of the period.

Figure 2 shows the total number of data samples, the median magnetic perturbation magnitudes, and the median local variability in the magnitudes (described below) during the weeklong period, plotted on a 110 km by 110 km equal-area grid in APEX coordinates, poleward of ±45° latitude in the Northern and Southern Hemispheres. Data coverage is available over this entire region in the Southern Hemisphere (where the offset between the magnetic and geographic poles is larger), and only small gaps are observed in the midlatitude region of the Northern Hemisphere. Due to the geometry of the orbits, the spatial coverage improves and the data counts increase toward the poles. In the Northern Hemisphere (the winter hemisphere during the study period), the magnetic perturbations tend to be largest in the nightside auroral region. In the Southern (summer) Hemisphere, on the other hand, the perturbations tend to be largest over the dayside polar cap.

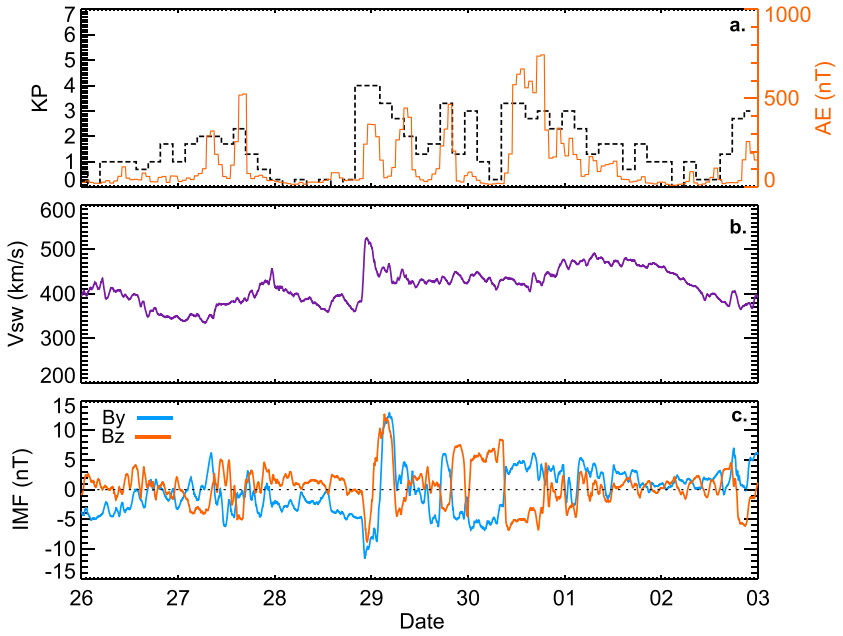

Figure 1. Time series for 26 November to 2 December 2011 of (a) the planetary (*Kp*) and auroral (*AE*) geomagnetic activity indices, (b) the earthward component of the solar wind velocity, and (c) the *y* and *z* components of the IMF in geocentric solar magnetospheric coordinates.

The local variability in the perturbation magnitudes (which is used as an estimate of uncertainly as described below) tends to be largest in the auroral regions in both hemispheres and the variability magnitudes are typically at least 50% of the perturbation magnitudes. The large increase in the uncertainty magnitudes near the equatorward edges of the plots is not a feature in the original data but is the result of including a latitude-dependent factor in the uncertainty estimate, as described below.

The uncertainty in the observed magnetic perturbations (as shown in Figures 2c and 2f) is not yet provided by the AMPERE Science Data Center (which provides a quality flag), so for this study the uncertainty is estimated directly from the perturbation data set using a multistep process described here. The week-long data set is searched for data points with at least five neighboring data points in the surrounding 2.5° latitude by 15° longitude region during the same 10 min time period (using nonoverlapping time steps). This criterion is selected based on the spatial and temporal resolution of the analysis described in the remainder of the paper and is typically met near spacecraft conjunctions or when high-rate data are available. The standard deviation of each collection of neighboring magnetic perturbation values is then calculated (treating the two horizontal vector components independently) and assigned as the uncertainty value of the central data point.

For data points with fewer than five neighboring data points, the local variance cannot be calculated and therefore uncertainty values must be prescribed. In this case, the uncertainties are set to a constant value, which is the median of all the standard-deviation-based uncertainty values (treating the two perturbation vector components independently). These prescribed uncertainty values are then multiplied by the AMPERE-provided quality flag, which ranges between ~0.7 and ~1.3 (smaller values indicate higher quality). The uncertainty values resulting from this process are almost entirely greater than 30 nT, consistent with the 30 nT resolution of the engineering-grade magnetometers, and most are less than 100 nT.

As an additional step for this study, all the uncertainty values described above are multiplied by a factor $(\sqrt{1+\exp((55-|\lambda|)/5.})$, where λ is latitude) that increases strongly with decreasing absolute latitude equatorward of 55°. This latitudinal adjustment is made because it has been observed that the AMPERE magnetic perturbation values do not tend toward zero with decreasing latitude, but rather remain large, a behavior that is not observed in data from other satellites and is likely unphysical [*Knipp et al.*, 2014]. Note that other formulations for increasing the uncertainty at lower latitudes were also tried, and it was found that the particular details of the adjustment do not have a significant impact on the final results.

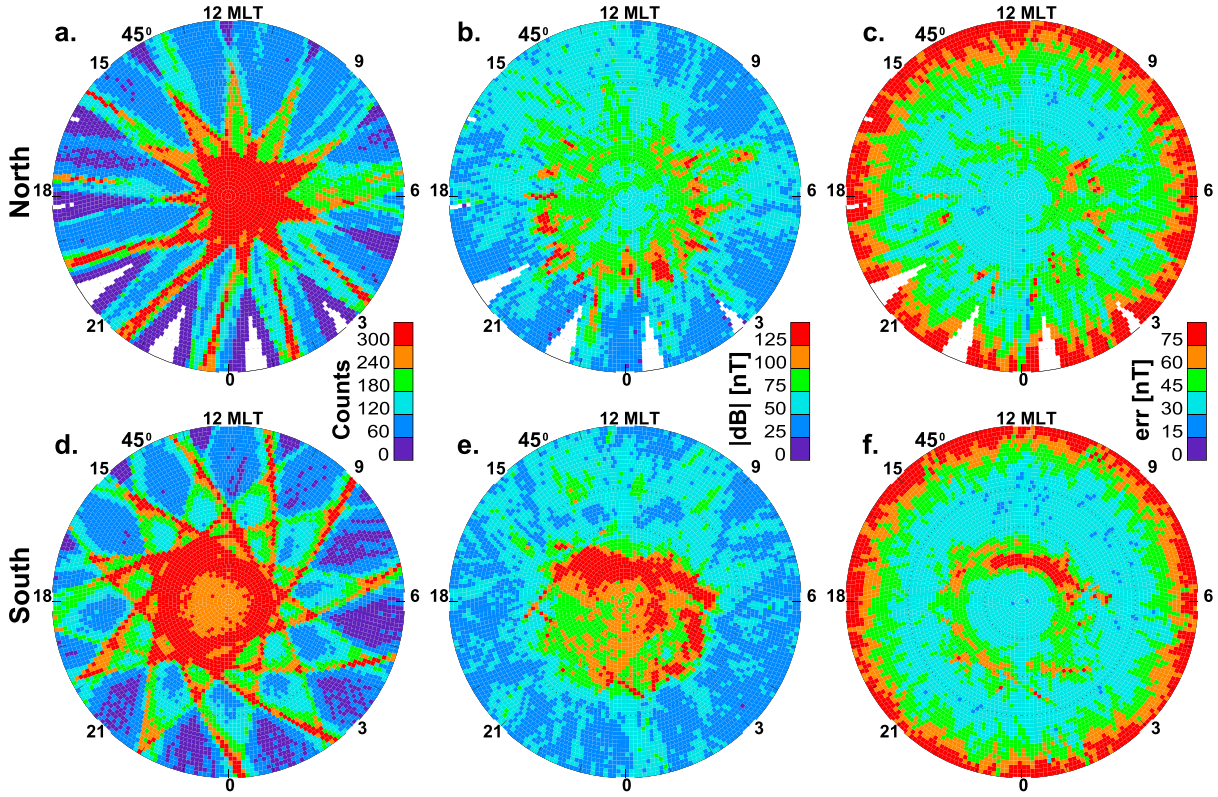

Figure 2. (a,d) Total number of data samples, (b,e) median magnetic perturbation magnitudes, and (c,f) median estimated uncertainty during 26 November to 2 December 2011, plotted on a 110 km by 110 km equal-area grid in APEX coordinates, poleward of ±45° latitude in the Northern (Figures 2a–2c) and Southern (Figures 2d–2f) hemispheres.

2.2. Calculating Empirical Orthogonal Functions

The AMPERE data set described in section 2.1 is analyzed using the method of EOFs, closely following the techniques used by *Cousins et al.* [2013] and *Matsuo et al.* [2002]. In the method of EOFs, the deviations of the observations from their mean state are decomposed into a set of finite, orthogonal modes of variability (EOFs), ordered by their contribution to the total variance in the observations. This technique is described in detail by *Cousins et al.* [2013] and is described briefly here.

Note that to keep this analysis tractable, we assume that the two-dimensional magnetic perturbation vectors are purely toroidal (i.e., that the relatively small poloidal component produced mainly by the auroral electrojets can be ignored) and can be represented by a spatial distribution (in latitude and longitude) of magnetic vector potential (using only the radial component):

$$\delta\vec{B}(\lambda,\phi) = \nabla \times (\hat{r}A_r(\lambda,\phi)), \tag{1}$$

where λ and ϕ are magnetic latitude and longitude, respectively. These assumptions are equivalent to those made by *Waters et al.* [2001] and *Weimer* [2001b].

Furthermore, the distribution of magnetic vector potential, $A_r(\lambda,\phi)$, is represented by a finite set of modified spherical cap harmonic basis functions. In particular, following the work of *Matsuo et al.* [2002] and *Cousins et al.* [2013], 60 basis functions are employed, and these functions are a linear combination of the basis functions developed by *Richmond and Kamide* [1988] (except that the colatitude of the edge of the spherical cap is 40° instead of 34° and the maximum longitudinal wave number is 12 instead of 10). Specifically, the set of basis functions consists of the first 60 principal components of the background error covariance matrix, "$\mathbf{C_u}$", also developed by *Richmond and Kamide* [1988]. (Taking principal components of "$\mathbf{C_u}$" provides a physically meaningful way to obtain a reduced set of basis functions, which is computationally preferable to using the full, original set of 244 functions.) These basis functions have a maximum resolution of 2.5° in latitude and 15° in longitude. The basis functions are normalized such that their horizontal gradients on a unit sphere have a root-mean-square value of 1, as described by *Richmond and Kamide* [1988].

Using this set of basis functions, the mean magnetic perturbation values can be described as follows,

$$\delta\vec{B}^{(\mathrm{mean})}(\lambda,\phi) = \sum_{k=1}^{n}\left[\beta_k^{(\mathrm{mean})}\nabla\times(\hat{r}X_k(\lambda,\phi))\right], \tag{2}$$

where X_k is the kth basis function and β_k is the coefficient of the kth basis function. The basis function coefficients $\beta^{(\mathrm{mean})}$ used to represent the mean distribution are estimated from the entire data set using weighted linear regression, with weights given by the inverse observational uncertainties.

The mean magnetic perturbations, as defined above, are subtracted from the entire data set and the residuals are analyzed using weighted nonlinear regression to obtain a set of 10 EOFs. As for the mean distribution, the EOFs are expressed in terms of magnetic vector potential and are represented by an expansion of basis functions. Each EOF minimizes the cost function, $L^{(\nu)}$, given by

$$L^{(\nu)} = \sum_j\sum_i\left|\vec{w}_{ij}\cdot(\vec{Y}_{ij}^{(\nu)} - \alpha_j^{(\nu)}\delta\vec{B}^{(\nu)}(\lambda_{ij},\phi_{ij}))\right|^2, \tag{3}$$

$$\vec{Y}_{ij}^{(\nu)} = \delta\vec{B}_{ij}^{(\mathrm{obs})} - \delta\vec{B}^{(\mathrm{mean})}(\lambda_{ij},\phi_{ij}) - \sum_{\gamma=1}^{\nu-1}\alpha_j^{(\gamma)}\delta\vec{B}^{(\gamma)}(\lambda_{ij},\phi_{ij}), \tag{4}$$

$$\delta\vec{B}^{(\gamma)}(\lambda,\phi) = \sum_{k=1}^{60}\beta_k^{(\gamma)}\nabla\times(\hat{r}X_k(\lambda,\phi)), \tag{5}$$

where $\delta\vec{B}_{ij}^{(\mathrm{obs})}$ and $\vec{w}_{ij}$ are two-dimensional magnetic perturbation observations and inverse observational uncertainties (based on variability), respectively, at the ith location at the jth time, $\alpha_j^{(\nu)}$ is the scaling factor (EOF coefficient) for time j, and the superscript ν indicates the EOF number (e.g., $\nu = 1$ indicates the first EOF). Each EOF is calculated using residuals, $\vec{Y}_{ij}^{(\nu)}$, obtained by subtracting the contribution of the mean and all previous, lower order EOFs from the original data. The basis function coefficients, $\beta_k^{(\nu)}$, that define the spatial form of the νth EOF are normalized to length 1 cTm and are required to be orthogonal to all previous EOFs. A more complete description of the calculation of the coefficients $\alpha_j^{(\nu)}$ and $\beta_k^{(\nu)}$ from the data is given by *Cousins et al.* [2013]. As in the analysis of *Cousins et al.* [2013], a 10 min time resolution is used for the EOF analysis. This time resolution allows for complete AMPERE data coverage (each orbit plane is completely sampled in 9 min) and enables direct comparison with the results described by *Cousins et al.* [2013].

The mean and first two EOFs calculated from the Northern Hemisphere AMPERE data set are shown in Figure 3, plotted as contours of magnetic vector potential in cTm for the mean (Figure 3a) and in normalized units (as described previously in this section) for the EOFs (Figures 3b and 3c). The mean distribution has a two-cell configuration with a maximum at dawn and a minimum at dusk; it will be shown that such a distribution of magnetic vector potential corresponds to a standard Region 1 (R1) and Region 2 (R2) field-aligned current configuration. The first EOF (Figure 3b) has a configuration similar to that of the mean but with additional midlatitude features. The second EOF (Figure 3c) also has a dominant two-cell configuration, but the dawn and dusk features extend to midlatitudes, additional features appear at the dayside and nightside of the auroral region, and higher-order longitudinal structure is observed toward the pole.

It should be noted that for the analysis described up to this point, both horizontal components of the observed magnetic perturbations are used, as is standard with the current (post-2010) version of the AMPERE data products [*Korth et al.*, 2010; *Anderson et al.*, 2014]. Analyses with the original, lower resolution Iridium data, however, used only the cross-track component of the magnetic perturbation vector. This selection was made because the impact of attitude uncertainties is greater in the along-track direction, resulting in increased measurement uncertainties in the along-track component of the magnetic perturbations [*Anderson et al.*, 2000]. To investigate the impact of using both vector components rather than just the cross-track component, the EOF analysis described earlier in this section is repeated using cross-track data alone and along-track data alone (using observational uncertainties calculated using the technique described in section 2.1).

Figure 4 shows the mean and first two EOFs calculated from cross-track data (Figures 4a–4c) and along-track data (Figures 4d–4f) independently, following the same format as in Figure 3. Significant differences are

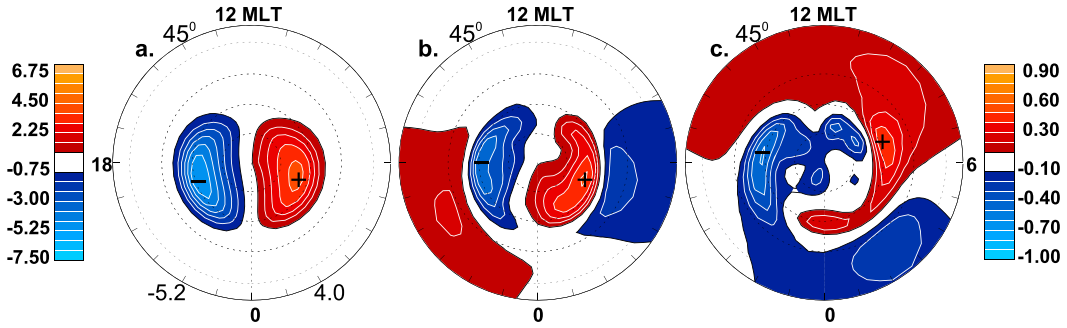

Figure 3. Contour plots of the radial component of magnetic vector potential for the (a) mean in cTm and (b and c) first two EOFs in normalized units, according to the color scales at left and right, respectively, plotted in geomagnetic latitude and local time. The maximum and minimum values are indicated at bottom right and bottom left, respectively, in Figure 3a.

observed between the two sets of EOFs, with clear high-latitude two-cell morphologies observed in the cross-track EOFs (Figures 4b and 4c) but not in the along-track EOFs (Figures 4e and 4f), which have more prominent midlatitude features. The power spectra for the two sets of EOFs are shown in Figure 4g, plotted as the relative contribution of the mean (denoted EOF 0) and each EOF to the total observed squared magnetic perturbations (δB^2). The spectrum for the along-track set of EOFs is significantly flatter than that for the cross-track set, with significantly less power captured by the mean and first EOF. A flatter spectrum is characteristic of noisy data, while a more peaked spectrum is characteristic of data containing more coherent signal. These results suggest that the along-track component of AMPERE data still contains significantly more measurement uncertainty than the cross-track component, and therefore, only the cross-track component of the data will be used for the analyses described in the remainder of this paper.

This choice to neglect the along-track data is not expected to have a significant impact on the final results. We expect that the vector magnetic data are dominated by a rotational component that can be expressed in terms of the rotated gradient of a scalar function A_r, as described above, and therefore, one component of the vector is, in principle, adequate to derive the scalar function (this assumption is consistent with prior studies, e.g., *Weimer* [2001b]). Including along-track data (if the quality is good) would roughly double the amount of information available for the fits and may sharpen somewhat the east-west gradients of the magnetic potential. It should be noted, however, that the spacecraft orbits are polar in geographic coordinates, and therefore, the cross-track data do sample north-south perturbations in magnetic coordinates. Furthermore, because the along-track component of the AMPERE data still contains significantly more measurement uncertainty than the cross-track data, they would contribute relatively little information to the fits if they are appropriately weighted by the inverse square of the error, even if they were included. This effect

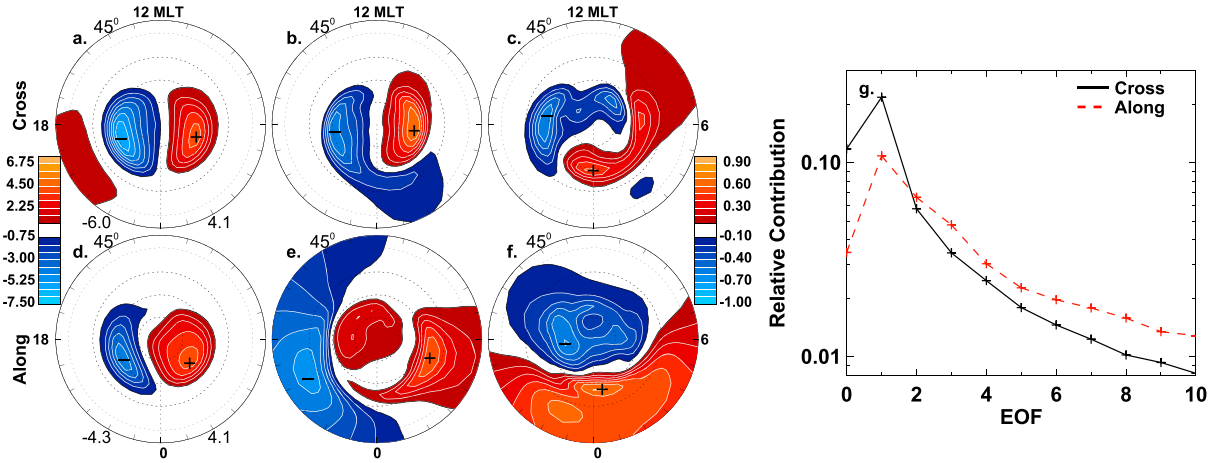

Figure 4. The mean and first two EOFs of magnetic vector potential calculated from (a–c) cross-track data and (d–f) along-track data, in the format of Figure 3. (g) The relative contribution of the mean (denoted EOF 0) and each EOF to the total observed δB^2, for both the cross- and along-track data.

can be seen by comparing Figures 3a (obtained using both components), 4a (obtained using cross-track data alone), and 4d (obtained using along-track data alone) and noting that the result obtained using both components is similar to the result obtained using cross-track alone.

3. Results

The technique described in section 2 is used to calculate mean distributions and EOFs independently for the Northern and Southern Hemispheres, in terms of magnetic vector potential, using only the cross-track component of the AMPERE data set. The mean and first three EOFs are shown in Figures 5a–5d for the north and in Figures 5e–5h for the south, in terms of radial current density above the ionosphere (which is assumed to be equivalent to FAC density), J_r, calculated as follows:

$$\mu_0 J_r = \hat{r} \cdot \nabla \times \delta\vec{B} = -\nabla^2 A_r, \tag{6}$$

where μ_0 is the permeability of free space and only the horizontal components of the Laplacian are included. The mean distributions shown in Figures 5a and 5e are plotted as contours of downward FAC density ($-J_r$) in $\mu A/m^2$, with the locations of maximum and minimum density indicated by "+" and "−" signs and the values given at bottom right and bottom left, respectively, and the total integrated downward FAC given at the top right. The format of the EOF plots (Figures 5b–5d and Figures 5f–5h) is similar, but the FAC density distribution has arbitrary sign and normalized units. Note that mean and EOFs shown in Figures 5a–5c are the same as those shown in Figures 4a–4c but with a different minimum latitude and plotted in terms of FAC density rather than magnetic vector potential. For each mean distribution and EOF shown (as well as the remaining EOFs not shown), the FAC density integrates to zero in the high-latitude region where it is defined, indicating that the upward and downward currents are balanced as expected.

The mean distributions in both hemispheres (Figures 5a and 5e), which represent the baseline states of the large-scale FAC distributions during the study period, show standard R1/R2 large-scale FAC morphology, with an R1 pair of poleward current structures into the ionosphere on the dawnside and out of the ionosphere on the duskside and an R2 pair of equatorward current structures of opposite directions [e.g., *Iijima and Potemra*, 1976]. In the Southern Hemisphere, the integrated downward FAC is larger than in the Northern Hemisphere and the peak current density is observed at dawn rather than at dusk as in the north.

The first EOFs in both hemispheres (Figures 5b and 5f) also show R1/R2 FAC morphology, although the features are more enhanced toward the dayside in the Southern Hemisphere than in the Northern Hemisphere. This EOF essentially captures a strengthening and weakening of the average FAC distribution, with positive contributions of this mode corresponding to strengthening.

The second EOF differs significantly between the two hemispheres. In the north, this EOF has a morphology similar to that of the typical R1/R2 system but modified by the addition of features on the dayside and nightside. This mode captures a mixture of effects, including the expansion and contraction of the average R1/R2 oval, the rotation of the pattern in MLT, and the wrapping of the FAC regions around the dayside and nightside. In the south, EOF 2 has a prominent pair of FAC features in the dayside cusp region, oppositely directed to each other. This mode captures the wrapping of the large-scale FAC regions around the dayside, with upward FAC at noon equatorward of downward FAC at noon for positive contributions of the mode.

The third EOF in both hemispheres contains mesoscale structure in both the meridional and zonal directions. Contributions of this mode to the global FAC distribution are more complex and not easily described.

Although interesting differences are observed between the means and EOFs in the two hemispheres, which will be discussed further in section 4, it is desirable to have a universal mean and universal set of EOFs that can be used to represent any AMPERE data (at least for the 1 week period of interest). Such a universal set is obtained by averaging the results from the two hemispheres using the EOF averaging technique employed by *Cousins et al.* [2013]. In this technique, covariance matrices are calculated in terms of the coefficients of the 244 *Richmond and Kamide* [1988] basis functions as

$$C_{lm} = \frac{1}{J-1} \sum_{j=1}^{J} \left[\sum_{\nu=1}^{N} \alpha_j^{(\nu)} \beta_l^{\prime(\nu)} \right] \left[\sum_{\nu=1}^{N} \alpha_j^{(\nu)} \beta_m^{\prime(\nu)} \right], \tag{7}$$

where the primed notation signifies that $\beta_l^{\prime(\nu)}$ is expressed in terms of the full 244 basis functions rather than the 60 dominant principal components as described in section 2, N is the total number of EOFs ($N = 10$), and J

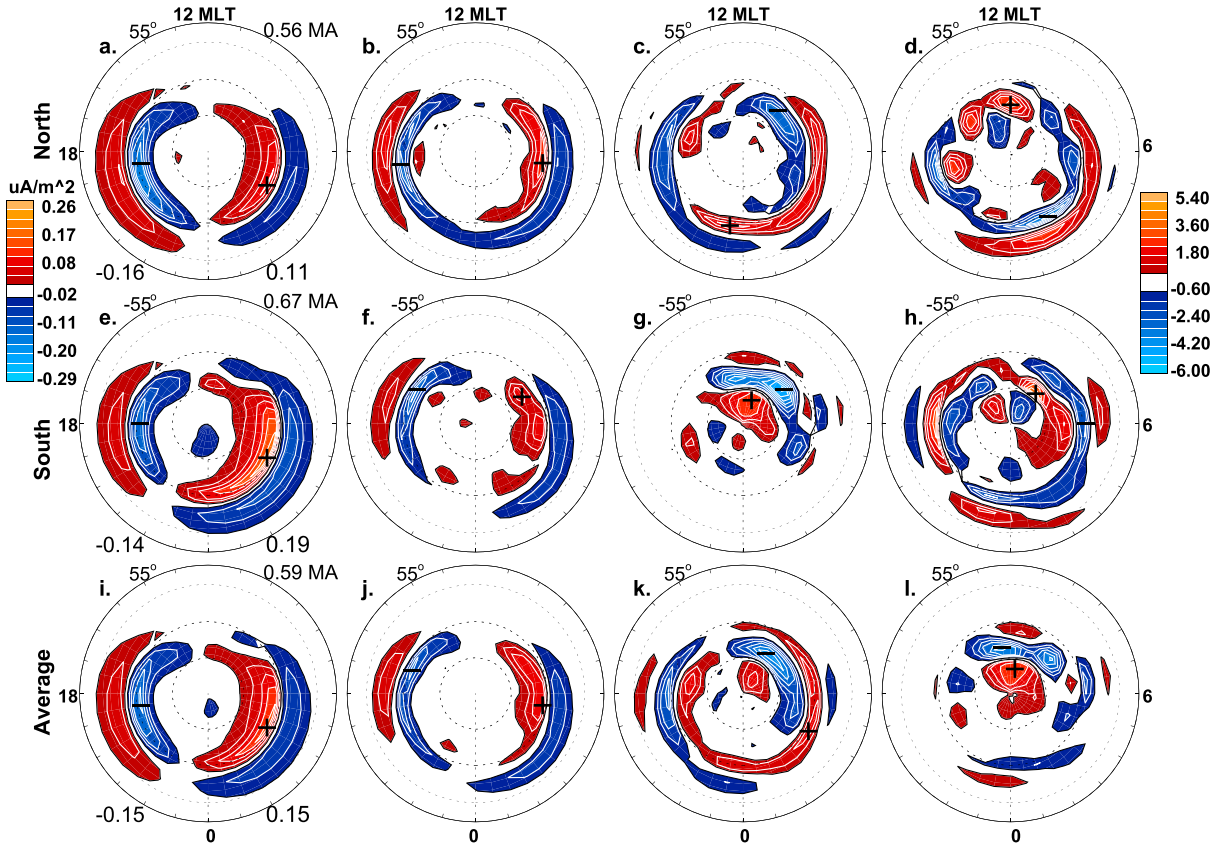

Figure 5. Contours of FAC density for the mean and first three EOFs for the (a–d) Northern Hemisphere, (e–h) Southern Hemisphere, and (i–l) average (described in text), in the format of Figure 3 but in terms of downward FAC (also note the change in minimum latitude). The total integrated downward FAC is indicated at the top right in Figures 5a, 5e, and 5i.

is the total number of times available. The covariance matrices calculated from the two individual sets of EOFs and their coefficients are averaged, and principal components of this average covariance matrix are calculated and defined to be the average or universal EOFs. To compute the universal mean, the mean distributions from the two hemispheres are simply averaged.

The universal mean and first three universal EOFs are shown in Figures 5i–5l, following the same format as in the figures for the individual hemispheres (Figures 5a–5d and 5e–5h). The universal mean and first EOF (Figures 5i and 5j, respectively) closely resemble the means and first EOFs from both hemispheres. The second universal EOF (Figure 5k) closely resembles EOF 2 from the Northern Hemisphere while the third universal EOF (Figure 5l) closely resembles EOF 2 from the Southern Hemisphere.

Figure 6a shows the relative contribution of the universal mean (denoted EOF 0) and 10 universal EOFs to the total observed δB^2 from the two hemispheres and the overall data set, plotted on a logarithmic scale. The mean and the first EOF contribute approximately 10% and 20%, respectively, to the total δB^2 in both hemispheres. EOF 3 (which contains prominent cusp features) captures significantly more variance in Southern Hemisphere data than in Northern Hemisphere data. The contributions of higher-order EOFs are significantly smaller and fall off quickly with increasing order.

The cumulative fraction of the observed δB^2 explained by the universal mean and the EOFs is shown in Figure 6b, with the northern and southern data again plotted separately. The universal mean and EOFs are capable of capturing approximately the same fraction of observed δB^2 in both hemispheres. The mean and 10 EOFs together account for 44% of the total observed δB^2. Note, however, that the observational uncertainty as estimated in section 2.1 accounts for 25% of the total observed δB^2, such that the set of EOFs likely accounts for more than 44% of the purely geophysical variations. If the total observed δB^2 is composed of 25% noise and 75% geophysical variations, then the set of EOFs accounts for 59% of the geophysical variations.

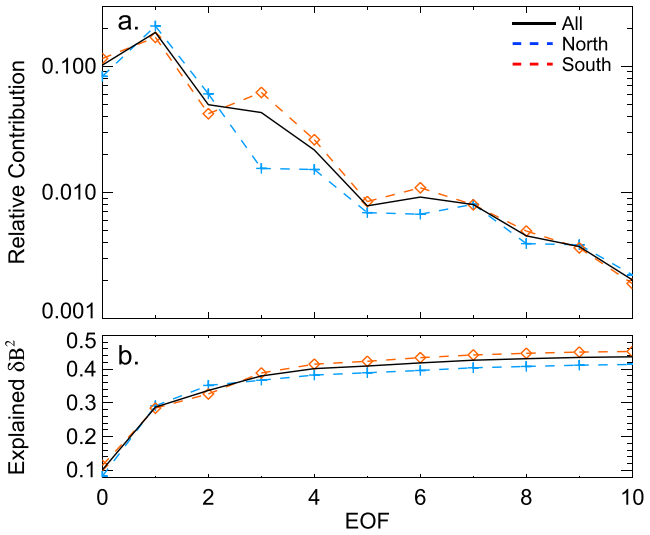

Figure 6. The (a) individual and (b) cumulative contributions of the universal mean (denoted EOF 0) and EOFs to the total observed δB^2 in the two hemispheres and in the total data set. Note the logarithmic scale in (a).

The universal covariance matrix defined earlier in this section also provides information regarding the spatial correlation scales of magnetic perturbations. As described by *Cousins et al.* [2013], this covariance matrix, which is expressed in terms of basis function coefficients, can be directly mapped to a covariance matrix for a spatial distribution of the geophysical variable of interest—magnetic perturbations in this case. This spatial covariance matrix is normalized to obtain a spatial correlation matrix, which describes the correlation between magnetic perturbations at different locations in the high-latitude region.

Figure 7 shows correlations in zonal magnetic perturbations along meridional and zonal paths about a point at (a) dawn and (b) noon at 68°magnetic latitude. From Figure 7, it is clear that correlation scales are highly anisotropic and vary significantly with location. At both dawn and noon, magnetic perturbations become uncorrelated quickly in the meridional direction. In the zonal direction, magnetic perturbations become uncorrelated very slowly near dawn and more quickly near noon, although in both cases (dawn and noon) the correlation scale is larger in the zonal direction than in the meridional direction. Note that the zonal resolution of the basis functions at the latitude shown in Figure 7 is somewhat larger than the meridional resolution, but the difference is small compared to the difference in correlation scales, suggesting that the anisotropy is geophysical and not an artifact of the analysis. The correlation behaviors shown in Figure 7 for dawn and noon sectors are similar to those for dusk and midnight sectors, respectively. Additionally, the features shown here for the universal covariance matrix are also seen in the results for both the Northern and Southern Hemispheres individually. Correlation scales for meridional magnetic perturbations (not shown) are more isotropic (i.e., more similar in the zonal and meridional directions) and uniform (i.e., less dependent on location) than those for zonal magnetic perturbations.

To investigate possible geophysical interpretations of the modes of variability (EOFs) calculated in this study, the EOF coefficients ($\alpha^{(\nu)}$) over the entire study time period are correlated to the values of various geophysical parameters. The best fit coefficients for the universal EOFs are estimated from the AMPERE data using an assimilative procedure described in Paper 2. The geophysical parameters considered are the *y* and *z* components of the IMF; the earthward component of the solar wind velocity; the dipole tilt (the angle between Earth's best fit dipole axis and the plane perpendicular to the Sun-Earth line, with positive angles toward the Sun in the Northern Hemisphere); and the auroral and global geomagnetic activity indices *AE*, *AL*, and *SYM-H*. Following *Cousins et al.* [2013], correlations are calculated using IMF and solar wind velocity data that have been averaged over 45 min, ending 10 min prior to the center of the 10 min resolution magnetic perturbation observation set. This averaging window was selected because it, in general, optimizes correlations with ionospheric observations, as described by *Weimer* [2005].

Table 1 gives correlation coefficient values for the six universal EOFs with the two parameters most strongly correlated with each EOF. (Correlations with *AL* are not shown because they are in all cases approximately

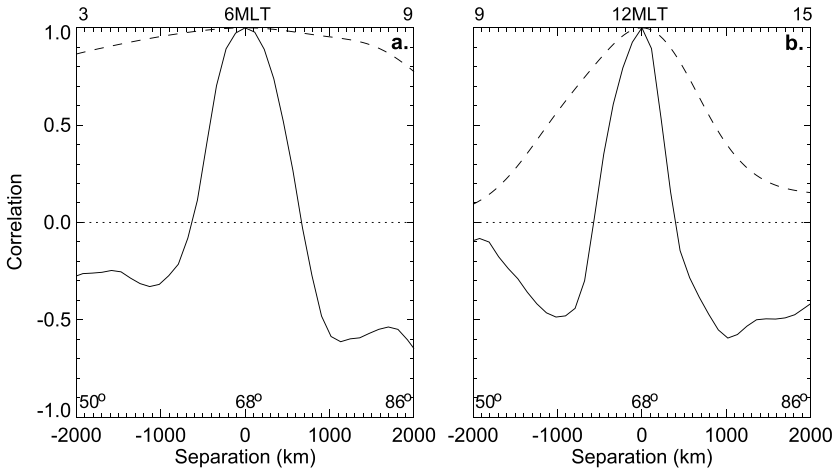

Figure 7. Correlation in zonal magnetic perturbations centered about (a) dawn and (b) noon at 68° magnetic latitude. Solid lines indicate meridional cuts (for latitudes given at bottom) and dashed lines indicated zonal cuts (for MLTs given at top) through the two-dimensional correlation function.

equal to correlations with *AE*.) Correlation coefficients are calculated and displayed separately for data from the two hemispheres, as well as for the complete data set. The 95% confidence interval in the correlation coefficient values is estimated (using bootstrap resampling, e.g., *Efron and Tibshirani* [1993]) to be ~0.1. EOF 1 is found to correlate strongly with *AE* and IMF B_z in both hemispheres, while EOF 2 is only weakly correlated with *AE* and is oppositely correlated with IMF B_y in the two hemispheres (even though the antisymmetrical response to IMF B_Y is accounted for by reversing the sign of IMF B_Y in the Southern Hemisphere). EOF 3 is strongly correlated to IMF B_Y in both hemispheres but more strongly in the south than in the north. The remaining EOFs are only moderately correlated, if at all, to geophysical parameters.

It should be noted that only a narrow range of geophysical conditions were present during the particular week considered in this study, and the EOF properties presented here are likely influenced to some extent by the characteristics of this week. Because the study period came near a solstice, winter-like and summer-like conditions are represented, but not equinox. Additionally, as shown in Figure 1, the study period contained predominantly quiet geomagnetic conditions, with only a moderate disturbance in the interplanetary medium impacting the geospace system. The planetary geomagnetic activity index *Kp* had a median value of 1+, a maximum value of 4, and was less than 3− for 77% of the time. Although the study period lacked any geomagnetic storm conditions, it is representative of typical geomagnetic conditions; e.g., the distribution of *Kp* values is approximately the same as that reported by *Cousins et al.* [2013] for January 2011 to August 2012.

Table 1. EOF Coefficient Correlations[a]

EOF	1	2	3	4	5	6
Mode	Strengthening	Expanding/Rotating	Cusp Shaping	-	-	-
			Correlations for Northern Data			
Top	*AE*: 0.91	B_Y: 0.25	B_Y: −0.56	*AE*: 0.34	V_{sw}: 0.11	B_Z: 0.26
2nd	B_Z: −0.64	*AE*: 0.22	*AE*: −0.46	B_Y: −0.20	B_Y: −0.09	AE: 0.26
			Correlations for Southern Data			
Top	*AE*: 0.82	*AE*: 0.25	B_Y[b]: −0.82	Tilt[c]: −0.30	B_Z: 0.40	Tilt[c]: 0.22
2nd	B_Z: −0.66	B_Y[b]: −0.24	Tilt[c]: −0.23	V_{sw}: −0.18	Tilt[c]: 0.40	*AE*: 0.19
			Correlations for All Data			
Top	*AE*: 0.84	*AE*: 0.24	B_Y[b]: −0.68	Tilt[c]: −0.35	B_Z: 0.24	B_Z: 0.12
2nd	B_Z: −0.63	*SYM-H*: −0.17	Tilt[c]: −0.25	*AE*: 0.14	*AE*: −0.11	Tilt[c]: 0.33

[a]Correlation coefficients are given for the two parameters that correlate most strongly with each EOF.
[b]The sign of IMF B_Y is reversed in the Southern Hemisphere.
[c]The sign of the dipole tilt is reversed in the Southern Hemisphere.

To characterize AMPERE data from time periods with geophysical conditions that are significantly different than the conditions found during the 1 week study period, new EOFs could be derived by repeating the technique described here for each new period, or a more universal set of EOFs could be derived by using the same technique but applied to a significantly larger data set than was available for this study.

4. Discussion

The results of the EOF analysis of AMPERE data described in section 3 are discussed in this section, specifically considering possible geophysical interpretations of the interhemispheric differences in results and of the correlations between the EOF coefficients and geophysical parameters. Additionally, the results are compared with those of previous EOF studies of high-latitude ionospheric data sets.

As described in section 3, several differences are observed between means and EOFs derived from Northern Hemisphere data and those derived from Southern Hemisphere data. (Note that the study period centers on 29 November, approximately 1 month prior to boreal winter solstice). Considering the mean distributions, the total integrated downward FAC density is larger by a factor of 1.2 in the Southern Hemisphere than in the Northern Hemisphere and the FAC densities are larger on the dawnside in the Southern Hemisphere while they are larger on the duskside in the Northern Hemisphere. Considering the EOFs, more nightside features are observed in the northern EOFs than in the southern EOFs, and EOF 2 has a different morphology in the two hemispheres. In the Southern Hemisphere, but not in the Northern Hemisphere, the second dominant mode of variability (EOF 2) is characterized by strong dayside cusp features; the coefficients of this EOF are correlated with IMF B_Y. Similarly, the third universal EOF (which is very similar to the Southern Hemisphere EOF 2) is more strongly correlated to IMF B_y in the south than in the north.

Differences that resemble those reported here have been observed in previous studies comparing winter and summer FAC distributions, regardless of hemisphere. Statistical studies of DE-2 [*Weimer*, 2001a, 2005], Ørsted and Magsat [*Papitashvili et al.*, 2002; *Christiansen et al.*, 2002], CHAMP [*Wang et al.*, 2005], and Iridium [*Green et al.*, 2009] data found that total integrated FAC magnitudes tend to be larger in summer than in winter by a factor ranging between 1.3 and 2. The factor of 1.2 found in this study is near this range and may be smaller than the previously observed values because the study period ends prior to the solstice. The previous statistical studies also found that summertime dayside FAC densities are especially enhanced, as compared to winter or nightside FAC densities, consistent with the stronger dayside features in the Southern Hemisphere in this study. In addition, both *Papitashvili et al.* [2002] and *Green et al.* [2009] noted that the impact of IMF B_Y on the FAC distribution tends to be larger in summer than in winter. This finding is consistent with observations in the current study of a stronger correlation between IMF B_y and universal EOF 3 in the south than in the north and the greater contribution of this EOF 3 to southern δB^2 than to northern δB^2.

Because the interhemispheric differences observed in this study are consistent with previously observed winter-summer differences, the observed differences are likely due, in large part, to seasonal effects on FAC properties rather than any asymmetries between the two hemispheres themselves (i.e., interhemispheric asymmetries in the geomagnetic field). These observed seasonal effects in FAC distributions can be attributed primarily to seasonal differences in the distribution of conductivity in the high-latitude ionosphere. The height-integrated conductivity (conductance) is significantly larger in the summer than in the winter, particularly on the dayside, which can be continuously sunlit during summer and continuously dark during winter. The enhanced summer conductances allow more currents to close through the ionosphere during summer than during winter. As suggested by *Papitashvili et al.* [2002] and *Green et al.* [2009], the difference in the strength of the IMF B_Y effect between summer and winter likely results from the suppression of FACs in the dayside polar cap (the region most effected by IMF B_Y) during winter due to low conductivity. The dawn-dusk asymmetries observed in this study (with opposite behaviors in the two hemispheres), however, is not clearly consistent with seasonal effects observed in previous statistical studies; the asymmetry may be the result of the particular IMF driving conditions that persisted during the week-long study period. A more thorough examination of interhemispheric and seasonal differences in FAC variability, taking into account dipole tilt and solar zenith angle (which likely have a more direct impact on FAC behavior than does pure season), is left to future work when a significantly larger data set is available.

The magnetic vector potential EOFs derived in this study based on AMPERE data have similar features to those of EOFs derived from other high-latitude ionosphere data sets, including electrostatic potential EOFs derived

from SuperDARN data by *Cousins et al.* [2013] and from DE-2 data by *Matsuo et al.* [2002] and FAC EOFs derived from CHAMP data by *He et al.* [2012]. As in this study, the results of both *Cousins et al.* [2013] and *He et al.* [2012] show that the first dominant mode of variability is the strengthening/weakening of the average pattern and the coefficients of this mode are correlated with IMF B_Z. The second dominant mode of variability in these two studies is the asymmetrical shaping of the pattern, primarily in the dayside/polar cap region, associated with the effects of IMF B_Y; this mode appears as EOF 3 in the current study. The results of *Matsuo et al.* [2002] also show a strengthening mode (correlated with IMF B_Z) and a shaping mode (correlated with IMF B_Y), but these modes appear as EOFs 2 and 1 rather than 1 and 2 (as seen by *Cousins et al.* [2013] and *He et al.* [2012]) or 1 and 3 (as seen in the current study). The second dominant mode of variability in the current study captures expanding/contracting and rotating of the average pattern and is weakly correlated with *AE*; this mode is similar to EOF 3 in the results of *Cousins et al.* [2013], which also captures expanding/contracting of the average pattern as is also correlated with *AE*.

In addition to the similarities between the modes of variability derived in this study and those derived from other data sets, strong similarities exist between the spatial correlation behaviors shown in Figure 7 for magnetic perturbations and those observed by *Cousins et al.* [2013] for electrostatic potential. The interpretation of these behaviors (longer correlation scales in the dawn and dusk regions than in the noon and midnight regions and longer correlations scales in the zonal direction than in the meridional direction) is discussed by *Cousins et al.* [2013]. In short, the cusp region is typically characterized by significant small-scale variability, while the dominant modes of large-scale variability (the first two EOFs) have large, coherent features in the dawn and dusk regions, consistent with longer correlation scales at dawn and dusk than at noon and midnight. Additionally, auroral zone features tend to be elongated in the zonal direction and narrow in the meridional direction [see *Cousins et al.*, 2013, and references therein], consistent with the longer correlation scales in the zonal direction observed in this study.

Although the individual EOFs are mathematical constructs and are not required to have any geophysical meaning, leading EOFs are often geophysically interpretable [*Wilks*, 2011; *von Storch and Zwiers*, 2002]. The strong correlations between the coefficients of EOFs 1 and 3 and IMF parameters and the strong similarities between these modes and modes of electric field variability suggest that these modes are, to a large extent, directly driven by external conditions. The effects of external drivers are not necessarily captured entirely by the first few EOFs but could appear in the remaining, higher-order EOFs as well. The higher-order EOFs could also capture variations not directly driven by external conditions (e.g., internal magnetospheric or ionospheric phenomena that are not immediately linked to changes in solar wind driving).

Although features in the universal EOFs derived in this study are similar to those in EOFs derived from other data sets, the AMPERE EOFs (along with the mean) in this study capture less observed variance than do EOFs (and means) for other data sets. In this study, the universal mean and first three EOFs account for 38% of the total observed δB^2 (not adjusting for the noise component of the variance); in the results of *Cousins et al.* [2013] and *Matsuo et al.* [2002], the mean and first three EOFs account for 51% and 54%, respectively, of the total observed E^2, while in the results of *He et al.* [2012] the mean and first three EOFs account for at least 65% of the total observed J_r^2.

The relatively large fraction of variance in AMPERE data that is not captured by the mean and the set of EOFs has several possible sources. In this study, unlike previous EOF analysis studies [*Matsuo et al.*, 2002; *Cousins et al.*, 2013], the mean accounts for less variance than does the first EOF. The reason for the small contribution of the mean in the AMPERE data is currently unknown. Another source of the unaccounted-for variance may be the result of large measurement uncertainties (noise) in the data resulting from the coarse resolution of the engineering-grade magnetometers and the uncertainties in attitude determination. As noted in section 2.1, the uncertainty values estimated for the AMPERE data are typically at least 50% of the magnitude of the observed magnetic perturbations. Similar relative uncertainty estimates for AMPERE data have also been obtained by *Knipp et al.* [2014] through an investigation of intra-AMPERE and AMPERE-DMSP discrepancies in magnetic perturbation observations. If, for example, 75% of the total δB^2 reported by AMPERE is geophysical variability, 51% of this variability is captured by the mean and the first three EOFs derived in this study.

Finally, another possible reason for the large magnetic perturbation variance that is not captured by EOFs is the quiet geomagnetic conditions that persisted for most of the study period. Due to this quiescence, the externally driven, large-scale component of the FAC system and the magnetic perturbation observations may be weak. This quiescence is unlikely to be the only explanation, however, because the geomagnetic conditions

during the study period are similar to those typically observed (as discussed in section 3), and the EOFs derived in previous studies, which did not select for geomagnetically active times, are able to account for a larger percentage of variance in the signal.

Given that the set of EOFs derived in this study captures a relatively small percentage of the total magnetic perturbation variance, some explanation of the utility of the technique may be desirable. While it is the case that a significant portion of the variance is not captured, it is the small-scale features and measurement noise that are not captured. On the other hand, it is the large-scale organized features that give the most information about SW-MI coupling and that affect the large-scale electrodynamic quantities in the polar regions, and the EOFs are an efficient way to represent these large-scale organized features. Specifically, comparing the EOFs to standard spherical cap harmonic (SCH) basis functions (using the basis functions developed by *Richmond and Kamide* [1988], described in section 2.2), the first three EOFs capture approximately twice as much variance as the first three SCH functions, and the first 10 EOFs capture approximately 1.5 times as much variance as the first 10 SCH functions.

Although differences are observed between EOFs derived independently for the two hemispheres, the set of universal EOFs is able to represent data from either hemisphere equally well. As shown in Figure 6, different universal EOFs capture more or less of the observations in the different hemispheres, but the full set of universal EOFs captures approximately the same fraction of the total observed δB^2 in both hemispheres. Furthermore, the same features in the spatial correlation patterns are seen in the results from the two hemispheres individually and in the average (universal) results. Given this result, the set of universal EOFs will be used as the basis of a covariance model in a data assimilation procedure for use with any AMPERE data (from the 1 week study period). This data assimilation procedure is described in Paper 2.

5. Summary

In this study, 1 week of AMPERE magnetic perturbation data are analyzed using the method of EOFs to identify dominant modes of variability in large-scale FACs. Through the use of this technique, the large-scale variability in FACs is quantified, correlations between the large-scale FAC variations and variations in possible external driving conditions are tested, and spatial correlations in FAC and magnetic perturbation variability are visualized and quantified. Only the cross-track component of the magnetic perturbations are included in the analysis because the along-track component of AMPERE data is found to contain significantly more measurement uncertainties than the cross-track component.

EOF analysis is applied independently to data from the Northern and Southern Hemispheres, which were in winter and summer, respectively, and differences are observed between the results from the two hemispheres. Specifically, the results show larger average FAC density, stronger dayside features, and more prominent IMF B_Y-related cusp variability in the Southern Hemisphere and differing dawn-dusk asymmetries in the two hemispheres. The observed interhemispheric differences are generally consistent with previously observed summer-winter differences in FACs, suggesting that seasonal differences in conductivity rather than interhemispheric geomagnetic asymmetries are the source of the observed differences in FAC properties.

A set of universal EOFs is derived by combining the hemispheric results, and the universal mean and first three universal EOFs account for 38% of the total observed δB^2 in either hemisphere. The mean distribution shows a standard Region 1/Region 2 FAC morphology and the first dominant mode of variability (EOF 1) captures a strengthening and weakening of this average pattern. EOF 1 is found to be well correlated with IMF B_Z ($r = -0.6$). The second mode of variability captures a mixture of effects, including expanding/contracting and rotating of the average FAC pattern, and is weakly correlated with the *AE* index ($r = 0.2$). The third mode of variability captures the wrapping of the Region 1/Region 2 FACs around the dayside cusp and is well correlated with IMF B_Y ($r = -0.7$). The properties of these universal EOFs are similar to those of EOFs derived from other data sets.

The first and third modes of variability, which are well correlated with IMF parameters, are likely directly driven by external conditions. The drivers of the remaining modes of variability are less clear, as the impact of these modes on the large-scale FAC morphology is more complex and weaker correlations with possible driving parameters are observed.

Combining the information from all the EOFs, a universal covariance matrix is obtained, which, among other applications, is used to estimate the spatial correlation scales of magnetic perturbations in the high-latitude

region. The correlation scales are found to be both highly anisotropic and nonuniform, with longer correlation scales seen in the zonal direction and near dawn and dusk.

In addition to describing properties of variability in large-scale FACs as observed by AMPERE, the results of the analysis described in this paper can be used in specifying error covariance for a data assimilation procedure for AMPERE data. This application is described in a companion paper [*Cousins et al.*, 2015].

Acknowledgments

We thank the AMPERE team and the AMPERE Science Center for providing the Iridium-derived data products. Instructions for obtaining these data can be found at http://ampere.jhuapl.edu/. We gratefully acknowledge the NASA Space Physics Data Facility; the World Data Center, Kyoto; and the National Geophysical Data Center for providing the high-resolution OMNI data; the *AE*, *AL*, and *SYM-H* index data; and the *Kp* index data, respectively. This work was supported by NSF grant AGS-1135446, AFOSR award 1210429, and NASA grant NNX13AD64G. T.M. is supported by NSF awards AGS-1025089 and PLR-1443703. The National Center for Atmospheric Research is sponsored by the National Science Foundation.

Larry Kepko thanks three anonymous reviewers for assistance evaluating this manuscript.

References

Anderson, B. J., K. Takahashi, and B. A. Toth (2000), Sensing global Birkeland currents with Iridium®; engineering magnetometer data, *Geophys. Res. Lett.*, *27*, 4045–4048.

Anderson, B. J., H. Korth, C. L. Waters, D. L. Green, and P. Stauning (2008), Statistical Birkeland current distributions from magnetic field observations by the Iridium constellation, *Ann. Geophys.*, *26*, 671–687.

Anderson, B. J., H. Korth, C. L. Waters, D. L. Green, V. G. Merkin, R. J. Barnes, and L. P. Dyrud (2014), Development of large-scale Birkeland currents determined from the Active Magnetosphere and Planetary Electrodynamics Response Experiment (AMPERE), *Geophys. Res. Lett.*, *42*, 3017–3025, doi:10.1002/2014GL059941.

Christiansen, F., V. O. Papitashvili, and T. Neubert (2002), Seasonal variations of high-latitude field-aligned currents inferred from ørsted and Magsat observations, *J. Geophys. Res.*, *107*, 1029, doi:10.1029/2001JA900104.

Clausen, L. B. N., J. B. H. Baker, J. M. Ruohoniemi, S. E. Milan, J. C. Coxon, S. Wing, S. Ohtani, and B. J. Anderson (2013), Temporal and spatial dynamics of the regions 1 and 2 Birkeland currents during substorms, *J. Geophys. Res. Space Physics*, *118*, 3007–3016, doi:10.1029/jgra.50288.

Cousins, E. D. P., T. Matsuo, and A. D. Richmond (2013), Mesoscale and large-scale variability in high-latitude ionospheric convection: Dominant modes and spatial/temporal coherence, *J. Geophys. Res. Space Physics*, *118*, 7895–7904, doi:10.1029/2013JA019319.

Cousins, E. D. P., T. Matsuo, and A. D. Richmond (2015), Mapping high-latitude ionospheric electrodynamics with SuperDARN and AMPERE, *J. Geophys. Res. Space Physics*, *120*, doi:10.1002/2014JA020463.

Efron, B., and R. J. Tibshirani (1993), *An Introduction to the Bootstrap*, Chapman & Hall/CRC, Boca Raton, Fla.

Green, D. L., C. L. Waters, B. J. Anderson, and H. Korth (2009), Seasonal and interplanetary magnetic field dependence of the field-aligned currents for both Northern and Southern Hemispheres, *Ann. Geophys.*, *27*, 1701–1715.

He, M., J. Vogt, H. Lühr, E. Sorbalo, A. Blagau, G. Le, and G. Lu (2012), A high-resolution model of field-aligned currents through empirical orthogonal functions analysis (MFACE), *Geophys. Res. Lett.*, *39*, L18105, doi:10.1029/2012GL053168.

Iijima, T., and T. A. Potemra (1976), The amplitude distribution of field-aligned currents at northern high latitudes observed by Triad, *J. Geophys. Res.*, *81*, 2165–2174.

King, J. H., and N. E. Papitashvili (2005), Solar wind spatial scales in and comparisons of hourly Wind and ACE plasma and magnetic field data, *J. Geophys. Res.*, *110*, A02104, doi:10.1029/2004JA010649.

Knipp, D. J., T. Matsuo, L. Kilcommons, A. Richmond, B. Anderson, H. Korth, R. Redmon, B. Mero, and N. Parrish (2014), Comparison of magnetic perturbation data from LEO satellite constellations: Statistics of DMSP and AMPERE, *Space Weather*, *12*, 2–23, doi:10.1002/2013SW000987.

Korth, H., L. Dyrud, B. Anderson, C. L. Waters, and R. J. Barnes (2010), *Abstract #SM11A-1692 Presented at Fall Meeting*, AGU, San Francisco, Calif., AMPERE science data reduction and processing, 13–17 Dec.

Matsuo, T., A. D. Richmond, and D. W. Nychka (2002), Modes of high-latitude electric field variability derived from DE-2 measurements: Empirical Orthogonal Function (EOF) analysis, *Geophys. Res. Lett.*, *29*(7), 1107, doi:10.1029/2001GL014077.

Merkin, V. G., B. J. Anderson, J. G. Lyon, H. Korth, M. Wiltberger, and T. Motoba (2013), Global evolution of Birkeland currents on 10 min timescales: MHD simulations and observations, *J. Geophys. Res. Space Physics*, *118*, 4977–4997, doi:10.1029/jgra.50466.

Papitashvili, V. O., F. Christiansen, and T. Neubert (2002), A new model of field-aligned currents derived from high-precision satellite magnetic field data, *Geophys. Res. Lett.*, *29*, 1683, doi:10.1029/2001GL014207.

Richmond, A. D. (1995), Ionospheric electrodynamics using Magnetic Apex Coordinates, *J. Geomagn. Geoelectr.*, *47*, 191–212.

Richmond, A. D., and Y. Kamide (1988), Mapping electrodynamic features of the high-latitude ionosphere from localized observations: Technique, *J. Geophys. Res.*, *93*, 5741–5759.

von Storch, H., and F. W. Zwiers (2002), *Statistical Analysis in Climate Research*, Cambridge Univ. Press, Cambridge, U. K.

Wang, H., H. Lühr, and S. Y. Ma (2005), Solar zenith angle and merging electric field control of field-aligned currents: A statistical study of the Southern Hemisphere, *J. Geophys. Res.*, *110*, A03306, doi:10.1029/2004JA010530.

Waters, C. L., B. J. Anderson, and K. Liou (2001), Estimation of global field aligned currents using the Iridium®; system magnetometer data, *Geophys. Res. Lett.*, *28*, 2165–2168.

Weimer, D. R. (2001a), An improved model of ionospheric electric potentials including perturbations and application to the Geospace Environment Modeling November 24, 1996, event, *J. Geophys. Res.*, *106*, 407–416.

Weimer, D. R. (2001b), Maps of ionospheric field-aligned currents as a function of the interplanetary magnetic field derived from Dynamics Explorer 2 data, *J. Geophys. Res.*, *106*, 12,889–12,902.

Weimer, D. R. (2005), Improved ionospheric electrodynamic models and application to calculating Joule heating rates, *J. Geophys. Res.*, *110*, A05306, doi:10.1029/2004JA010884.

Wilks, D. (2011), *Statistical Methods in the Atmospheric Sciences*, Acad. Press, Oxford, U. K.